




# Structural and Nanomechanical Properties of Cu (In<sub>x</sub>Ga<sub>1-x</sub>)Se<sub>2</sub> Thin Films Fabricated by One-Step Sputtering

TALAAAT A. HAMEED,<sup>1,4</sup> MD ABDULLAH A. MAMUN,<sup>1,2</sup>  
WEI CAO,<sup>1</sup> HANI E. ELSAYED-ALI,<sup>1,3</sup>  
and ABDELMAGEED A. ELMUSTAFA<sup>1,2,5</sup> 

1.—Applied Research Center, Thomas Jefferson National Accelerator Facility, Newport News, VA 23606, USA. 2.—Department of Mechanical and Aerospace Engineering, Old Dominion University, Norfolk, VA 23529, USA. 3.—Department of Electrical and Computer Engineering, Old Dominion University, Norfolk, VA 23529, USA. 4.—Solid State Physics Department, Physics Research Division, National Research Centre, 33 El Bohouth St., Dokki, Giza 12622, Egypt. 5.—e-mail: aelmusta@odu.edu

The structural and nanomechanical properties of Cu(In<sub>x</sub>Ga<sub>1-x</sub>)Se<sub>2</sub> films deposited on Si(100) substrate at different temperatures (25°C to 500°C) by one-step radiofrequency magnetron sputtering are discussed. X-ray diffraction analysis revealed a dominant (112) diffraction peak. The surface morphology was examined by field-emission scanning electron microscopy and atomic force microscopy. The film composition was examined by electron probe microanalysis. The Cu/(In + Ga) and Ga/(In + Ga) ratios were 0.9 and 0.3, respectively. Nanoindentation conducted in conjunction with scanning electron microscopy revealed that the films suffered severe delamination-type fracture due to poor adhesion to the Si substrate. The hardness of the films was not influenced by the substrate temperature except for the film grown at 500°C. The hardness was greatly affected at depths greater than the thickness of the film due to its poor adhesion. At deep indents, the hardness results agreed closely with that of the Si substrate.

## INTRODUCTION

Cu (In<sub>x</sub>Ga<sub>1-x</sub>)Se<sub>2</sub> (CIGS) thin films are used as an absorbing material in solar cells because their direct bandgap overlaps with the red end of the solar spectrum and they have a relatively high absorption coefficient ( $\alpha \sim 10^5 \text{ cm}^{-1}$ ).<sup>1</sup> The efficiency of CIGS solar cells has reached 23.35% for laboratory-scale devices and 15.7% for commercial modules,<sup>2</sup> the highest conversion efficiency among all commercial polycrystalline solar cells.<sup>3</sup> Their polycrystalline structure also makes them cost effective to fabricate on different substrates, including flexible thin metal and polymer sheets. By controlling the compositional gradient through the thickness of the CIGS absorbing layer, a conversion efficiency of 20.40% was demonstrated for a CIGS solar cell grown on flexible polymer sheet.<sup>4</sup>

CIGS thin films can be deposited by various techniques, such as coevaporation,<sup>5</sup> flash evaporation,<sup>6</sup> spray pyrolysis,<sup>7</sup> solution-based and electrodeless deposition,<sup>8</sup> closed-spaced vapor transport,<sup>9</sup> sputtering,<sup>10</sup> the sol-gel method,<sup>11</sup> and using nanoparticle ink solution.<sup>12</sup> For vapor-deposited CIGS, it is desirable to reduce the steps involved in order to reduce the time and cost of fabrication. A two-step vapor deposition process, based on deposition of Cu–In–Ga in the first step followed by selenization, has been extensively used.<sup>13</sup> This approach is suitable for large-scale production but the parameters of the post-selenization and annealing processes can greatly affect the quality of the resulting CIGS absorber layer. Several groups have studied fabrication of CIGS using one-step sputtering.<sup>14–17</sup> Addition of selenium is often required to optimize the stoichiometry of CIGS film.<sup>18</sup>

The structural, electrical, and optical properties of CIGS solar cell thin films have been intensively studied in the past.<sup>19–23</sup> However, the literature

(Received January 28, 2021; accepted June 10, 2021; published online June 22, 2021)

lacks research on the study of the mechanical properties of CIGS thin films. The significance of the mechanical properties is driven by the need to address fatigue failure due to thermal cyclic stress, delamination-type fracture due to poor adhesion to the substrate, and wear, which impacts the expected lifetime of CIGS solar cells. It is common practice to use the nanoindentation technique to characterize the mechanical properties of single- and multilayered films.<sup>18–20,24,25</sup> Among the mechanical properties of relevance to CIGS thin films are hardness, modulus, and fracture toughness. Nanoindentation has also been proved to be a helpful technique for characterizing the variation in the crystal structure and phase changes in thin films depending on their deposition parameters.<sup>26–29</sup>

The substrate temperature affects properties of thin films such as the adatom surface diffusion length, sticking coefficient, and grain growth. These in turn affect the surface morphology and film structure and composition. In the present study, substrate temperatures in the range from room temperature to 500°C were used. The highest value of 500°C is near the softening point of glass, which is the practical temperature limit when growing CIGS on commonly used glass substrates. Stoichiometric CIGS thin films were deposited using radiofrequency (RF) sputtering from a single quaternary CIGS target without addition of selenium or post-deposition annealing. The effect of the substrate temperature during deposition on the composition, structure, morphology, and nanomechanical properties of the CIGS thin films was then examined.

## EXPERIMENTAL PROCEDURES

CIGS thin films were deposited on Si(100) by one-step radiofrequency (RF) magnetron sputtering. Silicon wafers with miscut angle of 0.38°, *p*-type boron doped, and resistivity of 0.060 Ω cm to 0.075 Ω cm were used as substrates as provided by the manufacturer without further cleaning, so the surface contains native oxide. A 2-inch diameter CIGS target with Cu:In:Ga:Se composition of 0.24 at. %:0.25 at. %:0.05 at. %:0.51 at. % was used as the sputtering target. The chamber was first evacuated to the low 10<sup>-8</sup> Torr range. Sputtering was carried out in argon ambient with working pressure of 3 × 10<sup>-3</sup> Torr and argon flow rate of 20.3 SCCM. All thin films were sputtered with the magnetron operated at power of 85 W for 30 min and different substrate temperatures of 25°C, 150°C, 250°C, and 500°C. The structure of the films was examined using x-ray diffraction (XRD) analysis (MiniFlex II, Rigaku, Japan, Cu K<sub>α1</sub> irradiation, λ = 1.5406 Å). The composition of the films was determined by electron probe microanalysis (EPMA, Cameca SX100, Cameca, France). The film morphology was examined using scanning electron microscopy (SEM, JSM-600 LV, JEOL), field-emission scanning

electron microscopy (FESEM S-4700, Hitachi, Japan), and atomic force microscope (AFM, Dimension 3100, Veeco). The AFM images were taken in air in tapping mode.

The hardness of the CIGS films was measured using the XP CSM nanoindentation test method in depth control mode with a three-sided diamond Berkovich indenter tip.<sup>30</sup> The CSM test monitors the hardness and modulus as a continuous function of penetration depth. The G-Series CSM hardness, modulus, and tip cal method integrated into NanoSuite was employed to conduct the CSM tests on the samples. A series of maximum penetration depths of 100 nm, 200 nm, and 300 nm was maintained to ensure that the tip penetrated the film and also deep into the substrate, for the deep indents, to collect information about the properties from the surface to the substrate. A strain rate of 0.05 s<sup>-1</sup> was set for the loading rate with a peak hold time of 10 s during the tests. The allowable drift rate was set at 0.05 nm/s.

## RESULTS AND DISCUSSION

### Compositional Analysis

The chemical constituents present in the thin films were identified by electron probe microanalysis (EPMA). The compositions of the CIGS films was tested at five different locations on the film surface, and the values reported in Supplementary Table S1 are an average of the atomic percentage of each element. The error represents the standard deviation of the five measurements. All the thin films sputtered at different substrate temperatures had approximately the same composition. Comparing the sputtered films with the target, the average contents of Ga and Se increased while the average contents of Cu and In decreased for all the substrate temperatures. The compositions presented in Supplementary Table S1 show that the atomic percent ratios of Cu/(In + Ga) and Ga/(In + Ga) were ~ 0.9 and ~ 0.3 for all the films, corresponding to the compositions used for high-efficiency CIGS solar cells.<sup>1</sup>

### Structural Analysis

Figure 1 shows the XRD patterns of the CIGS films sputtered on silicon at substrate temperatures of 25°C, 150°C, 250°C, and 500°C. These patterns indicate that all the CIGS thin films showed narrow and intense peaks corresponding to polycrystalline structure. All CIGS thin films showed two dominant peaks, with a third peak appearing at substrate temperatures ≥ 150°C. These data are in good agreement with ICCD card no. 00-035-11020, with these peaks being indexed as (112), (204)/(220), and (116)/(312). No other peaks due to other phases were observed. The intensity of the (112) peak of the films deposited on Si(100) increased as the substrate temperature was increased from 25°C to 500°C. All

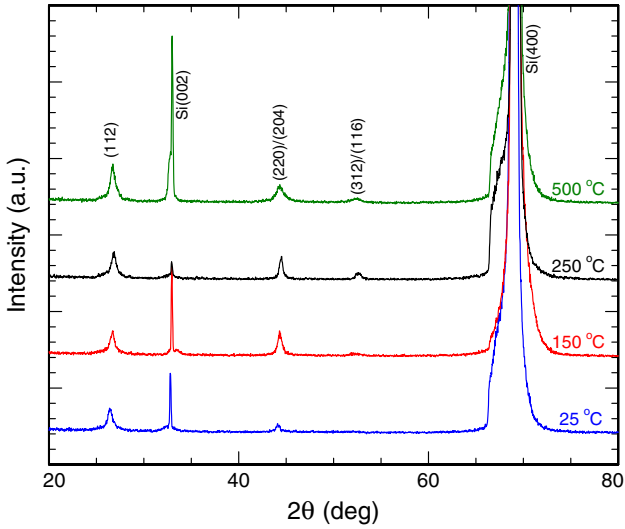


Fig. 1. XRD pattern of CIGS sputtered at different substrate temperatures on Si(100). The intensity of (112) reflection increases as the temperature increases.

the films showed a dominant diffraction peak corresponding to CIGS (112), indicating preferred (112) orientation.

The texture coefficient  $T_c(hkl)$  of the films under study was estimated as<sup>31</sup>

$$T_c(hkl) = \frac{I_0(hkl)}{I_s(hkl)} \left[ \frac{1}{N} \sum_{i=1}^n \frac{I_0(hkl)}{I_s(hkl)} \right]^{-1} \quad (1)$$

where  $I_0(hkl)$  is the observed intensity of the  $(hkl)$  diffraction peak,  $I_s(hkl)$  is the standard intensity, and  $N$  is the number of diffraction lines. Higher values of the texture coefficient for a specific plane indicate preferred orientation of the films. The data presented in Supplementary Table S2 show that the substrate temperature significantly affected the preferred orientation of the sputtered films, where the films were preferentially oriented along (112) direction when sputtered at substrate temperatures of 25°C and 500°C but (220)/(204) and (321)/(116) when sputtered at substrate temperatures of 150°C and 250°C, respectively. Such dependence of the texture on growth conditions was reported previously for vapor-deposited CIGS films,<sup>32</sup> where the texture was found to be highly dependent on the film composition; For example, a film with (112) texture had  $\text{Cu}/(\text{In} + \text{Ga}) = 0.79$ ,  $\text{Se}/(\text{Cu} + \text{Ga} + \text{Se}) = 1.07$ , and  $\text{Ga}/(\text{In} + \text{Ga}) = 0.26$ , while for a film with (220)/(204) texture, these ratios were 0.80, 1.09, and 0.28, respectively.<sup>32</sup> The substrate temperature affects the composition of the film and the surface diffusion of the adatoms during sputtering deposition. The sputtered CIGS texture was also shown to depend on the background pressure, which affected the  $\text{Cu}/(\text{In} + \text{Ga})$  ratio.<sup>33</sup>

The lattice parameters of the films were estimated from<sup>34</sup>

$$\frac{1}{d^2} = \frac{h^2 + k^2}{a^2} + \frac{l^2}{c^2} \quad (2)$$

The computed lattice parameters of the grown films are presented in Supplementary Table S2. The lattice parameters ( $a$ ,  $c$ ) are larger than the standard JCPDS data and decrease monotonically with increasing substrate temperature. Thus, the unit cell suffers tetragonal distortion along both  $a$ - and  $c$ -axes for films grown at lower substrate temperatures. As the substrate temperature was increased, the deformation decreased, as confirmed by the reduction of the  $c/a$  ratio, which reached its optimal value at 500°C. Accordingly, substrate heating is a key parameter for obtaining high-quality CIGS films, in agreement with previous studies.<sup>35,36</sup>

The average crystallite size  $D$  along the (112) direction was estimated from Scherrer's Eq.<sup>37</sup>

$$D = \frac{0.94\lambda}{\beta \cos \theta} \quad (3)$$

where  $D$  is the average crystallite size in nm,  $\lambda$  is the x-ray wavelength in nm,  $\theta$  is Bragg's angle, and  $\beta$  is the full-width at half-maximum (FWHM) of the diffraction peak. The average crystallite sizes of the films are listed in Supplementary Table S2. The average crystallite size increased from 13.0 nm for films deposited at 25°C to 13.9 nm for films deposited at 500°C. At elevated substrate temperatures, the atoms gain enough energy and mobility to settle at their ordered positions.<sup>38,39</sup>

### Film Morphology Studied by SEM

SEM images of the samples obtained at 25°C, 150°C, 250°C, and 500°C are shown for indents of 100 nm, 200 nm, and 300 nm in Figs. 2, 3, and 4, respectively. As the substrate temperature was increased, the features on the surface changed progressively and the corresponding structures grew larger. The 100-nm and 200-nm indents of Figs. 2 and 3 did not depict any delamination or fracture in any of the four samples. When the indentation depth was increased to 300 nm, the samples experienced significant delamination-type fracture. Note that, at first, cracks propagated along the edges of the indents, then the surrounding surface peeled off. The films collapsed locally in rose petal mode of fracture due to poor adhesion to the Si substrate. The size of the peeled-off surface was much larger than the size of the indent.

These experimental results reveal that radial cracks emerged at the 300-nm penetration depth for all four samples tested along all three edges of the indents. It was also evident that neither visible cracks nor delamination fractures were detected for the 100-nm or 200-nm indents. Since all the films were sputtered using the same power and duration, they all had the same thickness of  $200 \pm 10$  nm, as shown in the cross-sectional FESEM images in Fig. 5. This, obviously, indicates that the radial

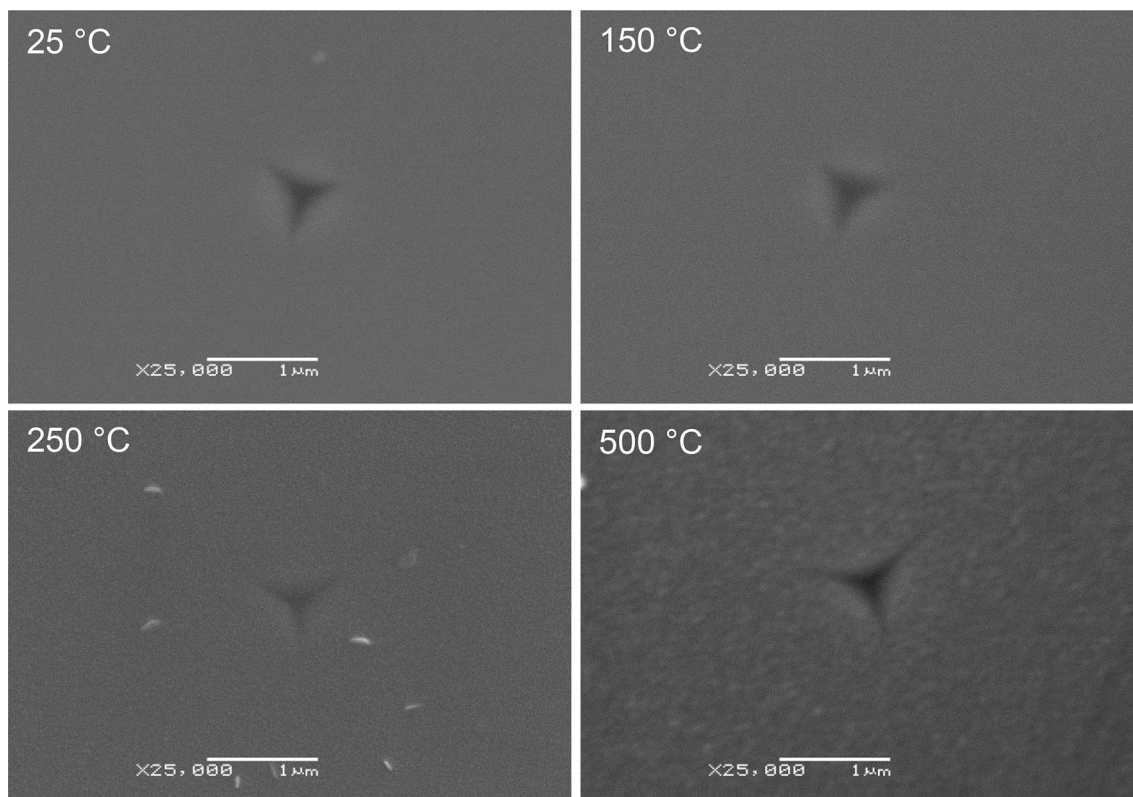


Fig. 2. SEM images of 100-nm indents on CIGS films on Si(100) sputtered at different substrate temperatures of 25°C, 150°C, 250°C, and 500°C.

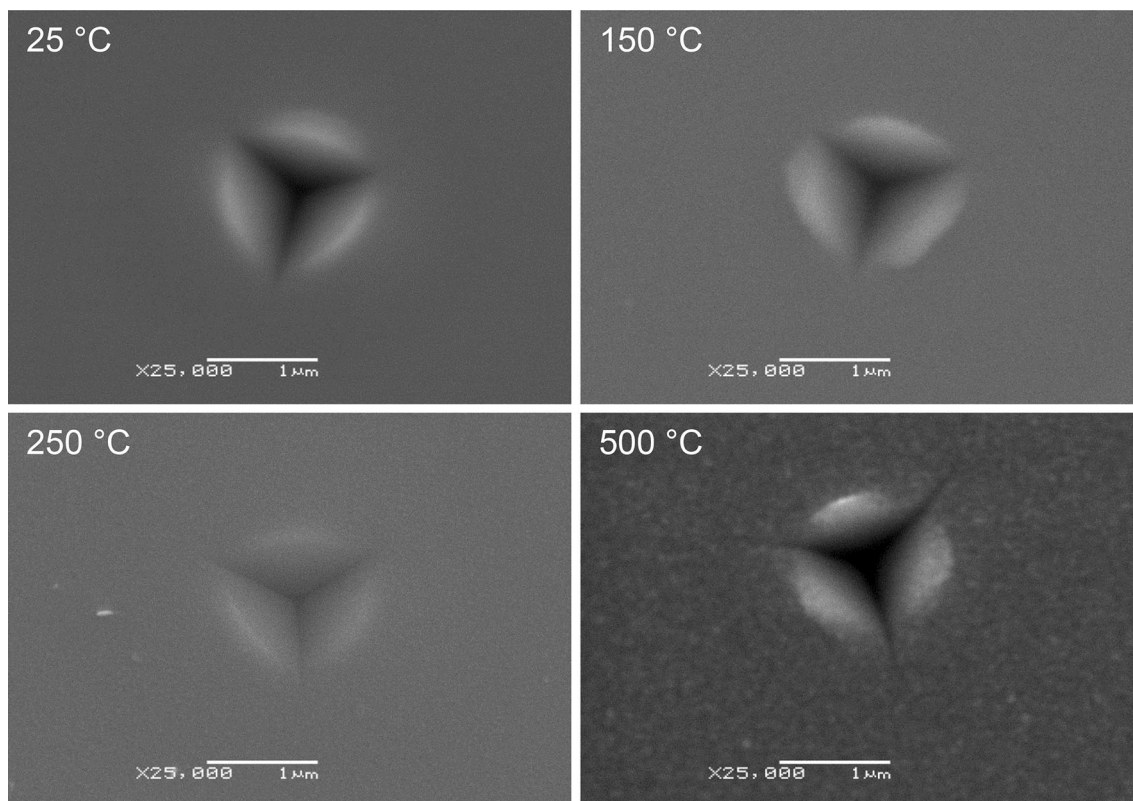


Fig. 3. SEM images of 200-nm indents on CIGS films on Si(100) sputtered at different substrate temperatures of 25°C, 150°C, 250°C, and 500°C.



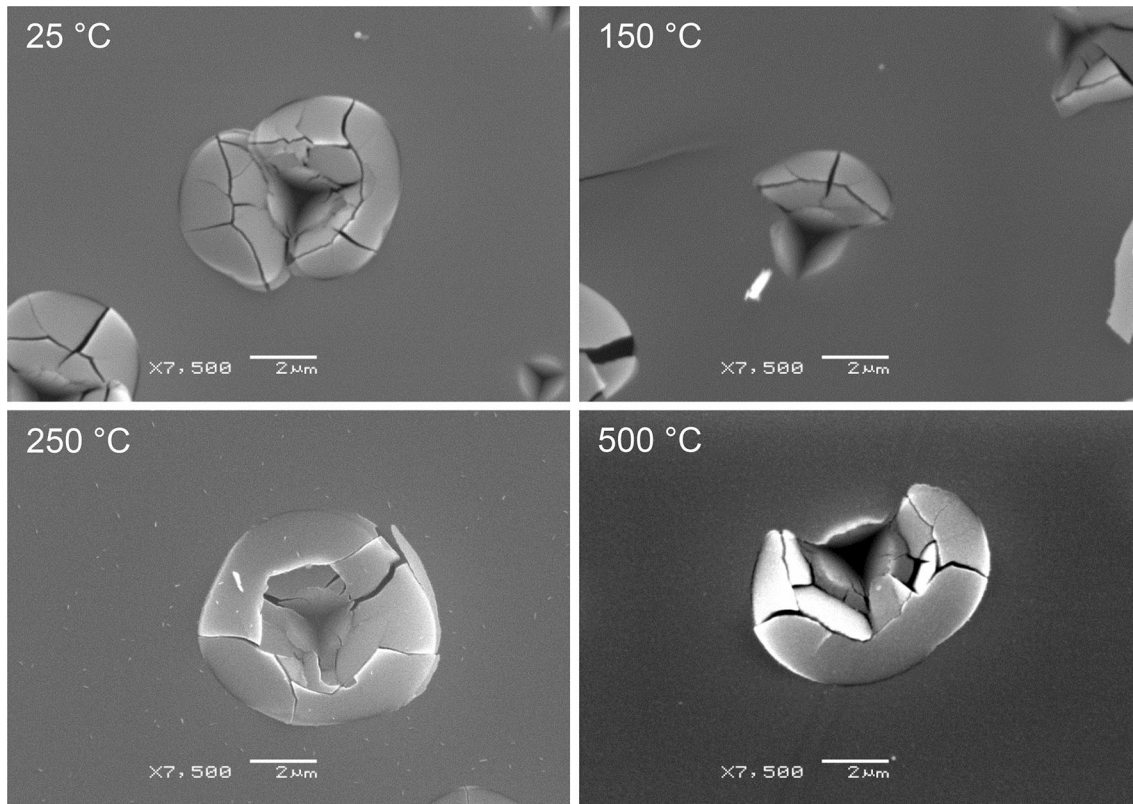


Fig. 4. SEM images of 300-nm indents on CIGS films on Si(100) sputtered at different substrate temperatures of 25°C, 150°C, 250°C, and 500°C.

cracks did not initiate at the film surface when the indenter tip established contact with the surface. Therefore, it can be concluded that the radial cracks initiated at the film–substrate interface and propagated upward to the surface of the four samples tested. This observation resembles earlier work by Karimi et al. when testing a number of TiAlN(Si,C) hard thin films.<sup>40</sup> However, all the samples exhibited the same trend of delamination fracture development.

### Surface Morphology Studied by AFM

Figure 6 shows AFM images of CIGS sputtered at different substrate temperatures. All the films showed well-defined polycrystalline grains. The root-mean-square (rms) surface roughness was measured to be 2.0 nm, 3.2 nm, 3.3 nm, and 5.2 nm for the samples obtained at 25°C, 150°C, 250°C, and 500°C, respectively. The increase in the surface roughness with increasing substrate temperature can be explained by the corresponding increase in the grain size. The individual grains were well identified in the AFM images, revealing grains of a few tens of nanometers, increasing with the deposition temperature, particularly for growth at 500°C. The topography of the thin film is also important as it has a direct effect on the performance of CIGS solar cells, because high surface roughness could result in incomplete coverage by

the CdS buffer layer between *p*-CIGS and *n*-ZnO, which could provide a shunt path.

### Nanoindentation Results

These results represent different indentation tests on the polycrystalline CIGS sputtered films on Si substrates. The hardness as a function of indentation depth is shown in Fig. 7. The subplot in Fig. 7 shows that the samples obtained at 25°C to 250°C exhibited the same hardness values of 6.5 GPa, whereas the sample obtained at 500°C depicted a lower hardness value of 5.5 GPa at a depth of 50 nm, which is less than 30% of the film thickness. The softness of the sample obtained at 500°C can be explained by the fact that the particulates grew larger at this higher temperature during deposition, which resulted in films with fewer defects, as is also evident from the SEM, FESEM, and AFM micrographs shown in Figs. 3, 5d, and 6d. The hardness continued to increase with increasing indentation depth up to 200 nm. The hardness suddenly dropped and then continued to increase again to reach the hardness of the Si substrate, except for the sample obtained at 500°C. The sudden drop in the hardness at indentation depths of more than 200 nm can be explained by the fact that the films suffered severe delamination fracture that initiated at the film–substrate interface, as explained in “[Film Morphology Studied by](#)

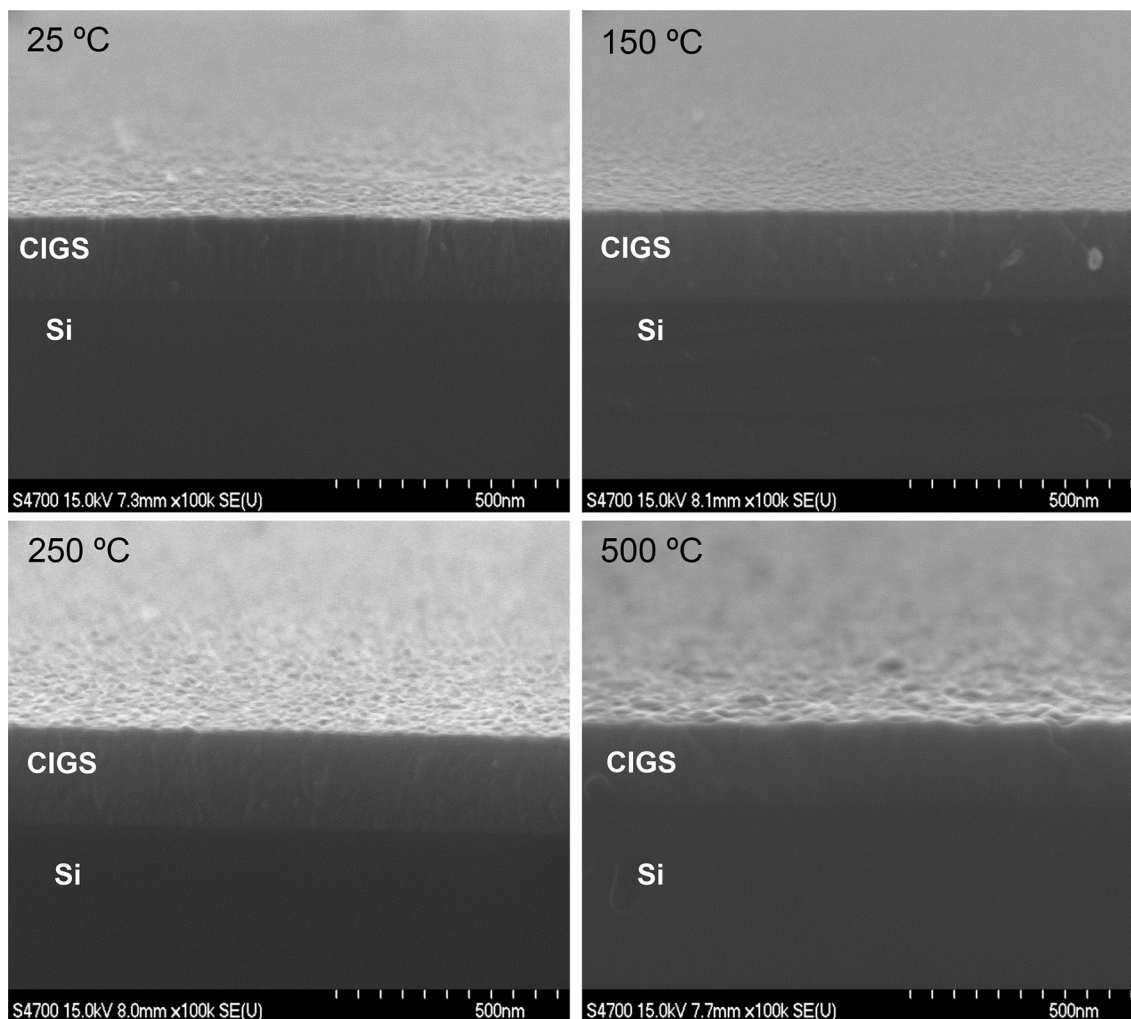


Fig. 5. Cross-sectional FESEM micrographs of CIGS films on Si(100) sputtered at different substrate temperatures of 25°C, 150°C, 250°C, and 500°C. All the films have the same thickness of  $200 \pm 10$  nm.

SEM" section and corroborated by the SEM images in Fig. 4. The sample obtained at 500°C was originally softer than the other films, which explains the absence of the sudden softening effect beyond an indentation depth of 200 nm.

It is evident that the samples obtained at 25°C to 250°C experienced significant delamination fracture during the loading cycle, as depicted in the SEM micrographs in Fig. 4, which can also be explained by the sudden drop in hardness. Although the sample obtained at 500°C exhibited delamination fracture, as indicated by the SEM images in Fig. 4, this is not reflected by the hardness measurements in Fig. 6. For the sample obtained at 500°C, it is possible that some degree of fracture occurred during the loading as a result of the less dense film due to grain coarsening (Figs. 5 and 6). However, the delamination fracture of the sample obtained at 500°C occurred mainly during the tip retraction from the surface, where the CSM protocol is unable to monitor the hardness during unloading (Fig. 4)

because the CSM protocol monitors the indenter tip progression and the hardness is calculated during the loading stage.

## CONCLUSION

The structural and nanomechanical properties of CIGS films deposited on Si(100) by one-step RF magnetron sputtering as a function of substrate temperature are reported. EPMA results confirmed that all the thin films sputtered at different substrate temperatures had approximately the same composition. XRD analysis revealed that all the films were chalcopyrite polycrystalline phase with a dominant diffraction peak corresponding to CIGS (112). Cross-sectional FESEM imaging confirmed a film thickness of 175 nm to 200 nm. SEM imaging of the residual impressions of indents showed the occurrence of delamination fracture for depths larger than the film thickness. AFM measurements showed that the surface roughness of the films



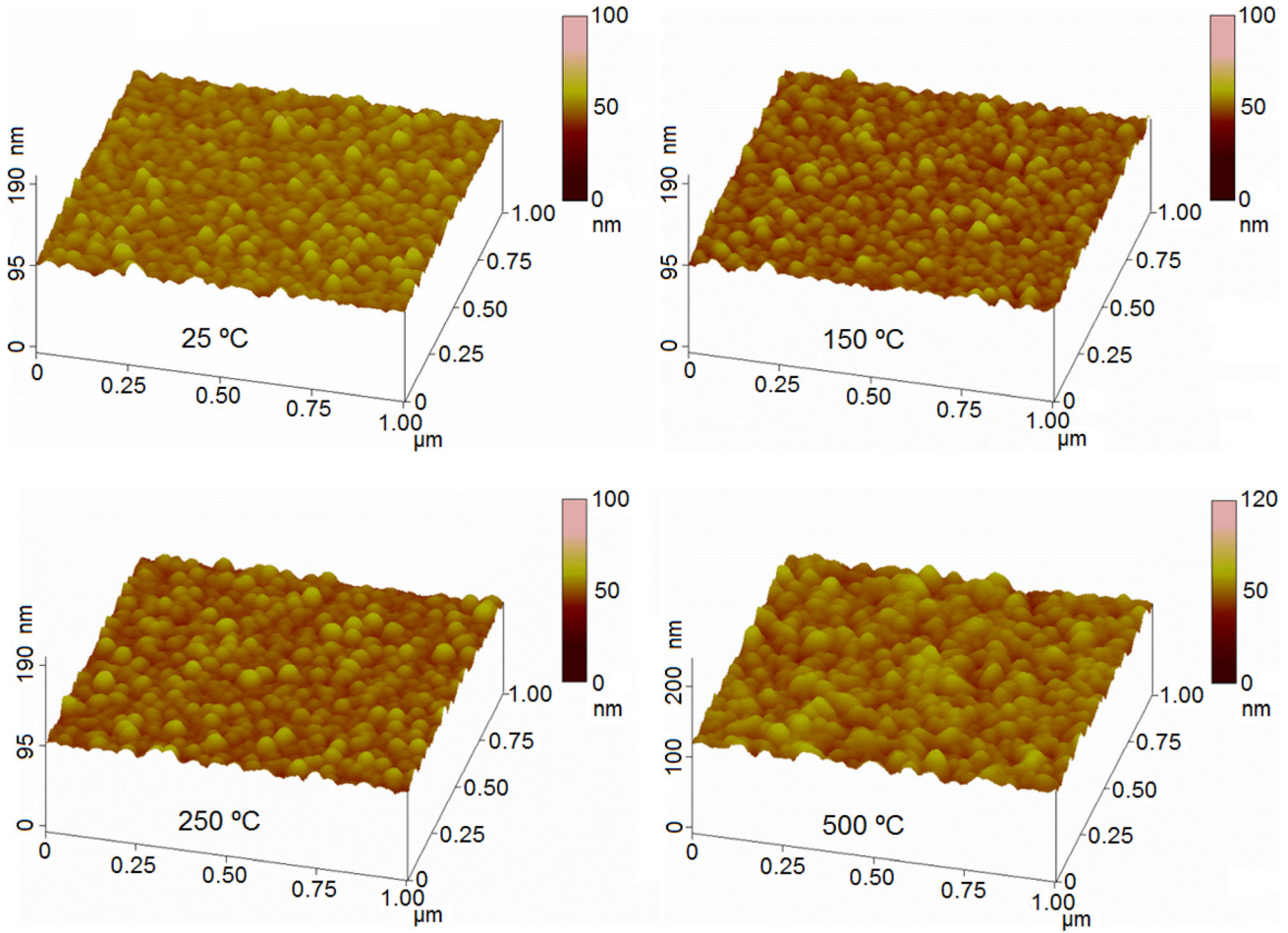


Fig. 6. AFM images of 200-nm indents on CIGS films on Si(100) sputtered at different substrate temperatures of 25°C, 150°C, 250°C, and 500°C. The root-mean-square (rms) roughness increased from 2.0 nm to 5.2 nm as the substrate temperature was increased.

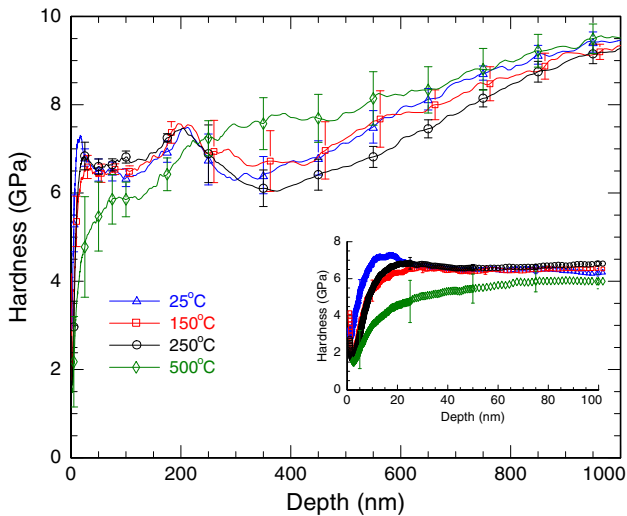


Fig. 7. Hardness versus indentation depth for CIGS films on Si(100) sputtered at different substrate temperatures of 25°C, 150°C, 250°C, and 500°C.

increased with increasing substrate temperature. AFM, SEM, and FESEM images clearly indicated the coarsening of the grains with increasing substrate temperature. From the nanomechanical investigation, the following observations were made: the samples obtained at 25°C to 250°C exhibited the same hardness of 6.5 GPa, whereas the sample obtained at 500°C showed a lower value of 5.5 GPa at a depth of 50 nm, which represents less than 30% of the film thickness; the samples obtained at 25°C to 250°C experienced delamination fracture during the loading cycle, which resulted in a sudden drop in the hardness values; for the sample obtained at 500°C, it is possible that some degree of fracture occurred during loading as a result of the less dense film due to grain coarsening; however, the delamination fracture of the sample obtained at 500°C occurred primarily during the tip retraction from the surface.

## ACKNOWLEDGEMENTS

This material is based on work supported by the Air force Office of Scientific Research and the National Science Foundation under grant no. MRI-0821180. T.A.H. was supported by the National Research Center, Egypt.

## CONFLICT OF INTEREST

On behalf of all authors, the corresponding author states that there are no conflicts of interest.

## SUPPLEMENTARY INFORMATION

The online version contains supplementary material available at <https://doi.org/10.1007/s11837-021-04764-1>.

## REFERENCES

- C.A. Wolden, J. Kurtin, J.B. Baxter, I. Repins, S.E. Shaheen, J.T. Torvik, A.A. Rockett, V.M. Fthenakis, and E.S. Aydil, *J. Vac. Sci. Technol. A* 29, 030801. (2011).
- M. Nakamura, K. Yamaguchi, Y. Kimoto, Y. Yasaki, T. Kato, and H. Sugimoto, *IEEE J. Photovolt.* 9(6), 1863–1867. <http://doi.org/10.1109/JPHOTOV.2019.2937218> (2019).
- M.A. Green, E.D. Dunlop, J. Hohl-Ebinger, M. Yoshita, N. Kopidakis, and X. Hao, *Prog. Photovolt. Res. Appl.* 28, 629–638. <https://doi.org/10.1002/pip.3303> (2020).
- A. Chirilă, P. Reinhard, F. Pianezzi, P. Bloesch, A.R. Uhl, C. Fella, L. Kranz, D. Keller, C. Gretener, and H. Hagerdörfer, *Nat. Mater.* 12, 1107–1111. (2013).
- W. Li, L. Yao, K. Li, X. Li, B. Yang, S. Xu, S. Shi, C. Yi, M. Chen, Y. Feng, and A.C.S. Appl. *Energy Mater.* 3, 4201–4207. (2020).
- P.S. Suryavanshi, H. Khunt, B. Rehani, and C.J. Panchal, *Mater. Today Proc.* 4, 12500–12504. (2017).
- S. Shirakata, Y. Kannaka, H. Hasegawa, T. Kariya, and S. Isomura, *Jpn. J. Appl. Phys.* 38, 4997–5002. (1999).
- R.N. Bhattacharya, J.F. Hiltner, W. Batchelor, M.A. Contreras, R.N. Noufi, and J.R. Sites, *Thin Solid Films* 361, 396–399. (2000).
- A. Bouloufa, K. Djessas, and D. Todorovic, *Mater. Sci. Semicond. Process.* 12, 82–87. (2009).
- J.A. Frantz, J.D. Myers, R.Y. Bekele, V.Q. Nguyen, B.M. Sadowski, S.I. Maximenko, M.P. Lumb, R.J. Walters, and J.S. Sanghera, *IEEE J. Photovolt.* 6, 1036–1050. (2016).
- U.C. Matur, and N. Baydogan, *J. Nanoelectron. Optoelectron.* 12, 352–358. (2017).
- M. Singh, P. Prasher, and K. Suganuma, *Nano-Structures Nano-Objects* 11, 129–134. (2017).
- T.-Y. Lin, C.-H. Chen, W.-C. Huang, W.-H. Ho, Y.-H. Wu, and C.-H. Lai, *Nano Energy* 19, 269–278. (2016).
- L. Oliveira, T. Todorov, E. Chassaing, D. Lincot, J. Carda, and P. Escribano, *Thin Solid Films* 517, 2272–2276. (2009).
- K. Kushiya, *Solar Energy Mater Solar Cells* 93, 1037–1041. (2009).
- K. Ellmer, J. Hinze, and J. Klaer, *Thin Solid Films* 413, 92–97. (2002).
- J.C. Park, M. Al-Jassim, S.W. Shin, J.H. Kim, and T.W. Kim, *Ceram. Int.* 45, 4424–4430. (2019).
- Z. Yu, Y. Yan, S. Li, Y. Zhang, C. Yan, L. Liu, Y. Zhang, and Y. Zhao, *Appl. Surf. Sci.* 264, 197–201. (2013).
- G. Pürçek, E. Bacaksız, and I. Miskioğlu, *J. Mater. Process. Technol.* 198, 202–206. (2008).
- T. Nakada, *Electron. Mater. Lett.* 8, 179–185. (2012).
- R.L. Garris, S. Johnston, J.V. Li, H.L. Guthrey, K. Ramathanan, and L.M. Mansfield, *Solar Energy Mater. Solar Cells* 174, 77–83. (2018).
- R. Mohan and R. Paulose, *Photoenergy Thin Film Mater.* 157–192. (2019).
- H. Shaban, S.A. Gad, B.A. Mansour, S.H. Moustafa, and T.A. Hameed, *J. Inorg. Organometall. Polym. Mater.* (2019).
- L.C. Andreani, P.A. Kowalczewski, C.I. Mura, M. Patrini, M. Acciarri, S. Binetti, A. Sassella, and S. Marchionna, *Towards CIGS Solar Cells with Reduced Film Thickness: A Study of Optical Properties and of Photonic Structures for Light Trapping*, pp. 2334.
- K. Tapily, J.E. Jakes, D.S. Stone, P. Shrestha, D. Gu, H. Baumgart, and A.A. Elmustafa, *J. Electrochem. Soc.* 155, H545. (2008).
- M.A. Al Mamun, A.H. Farha, Y. Ufuktepe, H.E. Elsayed-Ali, and A.A. Elmustafa, *J. Mater. Res.* 27, 1725. (2012).
- M.A. Hafez, M.A. Mamun, A.A. Elmustafa, and H.E. Elsayed-Ali, *J. Phys. D Appl. Phys.* 46, 175301. (2013).
- Y. Ufuktepe, A.H. Farha, S.-I. Kimura, T. Hajiri, F. Karadağ, M.A. Al Mamun, A.A. Elmustafa, G. Myneni, and H.E. Elsayed-Ali, *Mater. Chem. Phys.* 141, 393–400. (2013).
- Y. Ufuktepe, A.H. Farha, S.I. Kimura, T. Hajiri, K. Imura, M.A. Mamun, F. Karadag, A.A. Elmustafa, and H.E. Elsayed-Ali, *Thin Solid Films* 545, 601–607. (2013).
- G.M. Pharr, *Mater. Sci. Eng. A* 253, 151–159. (1998).
- J.R. Mohamed, C. Sanjeeviraja, and L. Amalraj, *J. Asian Ceram. Soc.* 4, 191–200. (2016).
- S. Chaisitsak, A. Yamada, and M. Konagai, *Jpn. J. Appl. Phys.* 41, 507–513. (2002).
- Y. Yan, F. Jiang, L. Liu, Z. Yu, Y. Zhang, and Y. Zhao, *Electron. Mater. Lett.* 12, 59–66. (2016).
- W. Chen, W. Cao, T.A. Hameed, S. Marsillac, and H.E. Elsayed-Ali, *J. Mater. Sci. Mater. Electron.* 26, 1743–1747. (2014).
- L. Zhang, Q. He, W.-L. Jiang, F.-F. Liu, C.-J. Li, and Y. Sun, *Solar Energy Mater Solar Cells* 93, 114–118. (2009).
- H. Wang, Y. Zhang, X.L. Kou, Y.A. Cai, W. Liu, T. Yu, J.B. Pang, C.J. Li, and Y. Sun, *Semicond. Sci. Technol.* 25, 055007. (2010).
- T.A. Hameed, S.H. Moustafa, H. Shaban, and B.A. Mansour, *Opt. Mater.* 109, 110308. (2020).
- T.A. Hameed, W. Cao, E.M. Abdelrazek, I.K. El Zawawi, B.A. Mansour, and H.E. Elsayed-Ali, *J. Mater. Sci. Mater. Electron.* 27, 3209–3216. (2015).
- T.A. Hameed, W. Cao, B.A. Mansour, I.K. Elzawaway, E.-M.M. Abdelrazek, and H.E. Elsayed-Ali, *J. Vac. Sci. Technol. A* 33, 031201. (2015).
- A. Karimi, Y. Wang, T. Cselle, and M. Morstein, *Thin Solid Films* 420, 275–280. (2002).

**Publisher's Note** Springer Nature remains neutral with regard to jurisdictional claims in published maps and institutional affiliations.